The International Journal of Advanced Manufacturing Technology (2019) 102:3747–3756
https://doi.org/10.1007/s00170-019-03499-3

ORIGINAL ARTICLE

Lateral powder transport model with Gaussian distribution in laser cladding

Xinyong Gong[1] · Junhong Wang[1] · Haimei Feng[1]

Received: 7 September 2018 / Accepted: 19 February 2019 / Published online: 26 February 2019

Abstract

Study on distribution characteristics of powder flux is helpful to improve stability during laser cladding. The definition of powder transport ratio is given by the mass ratio of powder particles fed into the molten pool to all powders transported in the process of laser cladding by lateral powder feeding. Based on law of mass conservation and kinematic equation in physics, a powder transport model for flow field with Gaussian distribution is established and a mathematical expression of powder transport ratio is proposed. Then, the model is applied to calculate cross-sectional area of clad layer formed by powders falling into the molten pool. Theoretical and experimental value have the same variation with process parameters, and modified theoretical value is much closer to the latter. Theoretical powder transport ratio is also confirmed by experimental powder capturing efficiency. So the powder transport model can be used for fundamental study of actual powder flow field. In addition, comparing with cylindrical type, Gaussian powder flow field is more realistic.

Keywords Laser cladding · Powder flow field · Gaussian distribution · Powder transport model · Cross-sectional area · Powder capturing efficiency

Nomenclature

Input variables of the model

D	Laser beam diameter
D_{jet}	Powder nozzle diameter
g	Gravity acceleration
L	Distance from nozzle to laser beam center in z-direction
P	Laser power
V_m	Powder feed rate
V_{P0}	Initial velocity of powders from nozzle
V_S	Laser scanning speed
W	Distance from nozzle to laser beam center in x-direction
φ	Divergence angle of powder flux
ρ	Density of clad material

Other model variables

$C_G(z_1)$	Mass distribution of powder particles with Gaussian flow field in unit distance of z_1-direction
$C_G(x_1,z_1)$	Concentration distribution for Gaussian flow field in the S_1 coordinate system
$f_G(x_1;\mu,\sigma)$	Density function for Gaussian distribution
L_{AO}	Distance from powder nozzle to laser beam center
m_3	Mass of powder particles stored on Q_3Q_4 segments
m_4	Mass of powder particles stored on Q_1Q_2 segments
$m(z_1)$	Mass of powder particles stored in dz_1 distance of z_1- direction within the space of flow field
M_{PT}	Mass of powders transported in clad layer per unit length
S	Cross-sectional area measured by experiment
S^G_{PT}	Theoretical cross-sectional area of clad layer
S_{P0}	Maximum of cross-sectional area as the powder transport ratio is 100%
V_0	Initial velocity of powder particles in z-direction
V_{PE}	Terminal velocity of powder particles
γ	The angle from straight-line trajectory of central particles to horizontal direction
φ_1	Positive divergence angle for powders falling on the molten pool boundary
φ_2	Negative divergence angle for powders falling on the molten pool boundary
ξ^G_{PT}	Transport ratio of powder flow field with Gaussian distribution
ξ_L	Powder efficiency for length
ξ_φ	Powder efficiency for angle

✉ Xinyong Gong
huagu1984@126.com

[1] School of Mechanical and Electrical Engineering, North China Institute of Science and Technology, No. 467 Xueyuan Street, Langfang 065201, People's Republic of China

μ Mathematical expectation of Gaussian distribution
σ Standard deviation of Gaussian distribution

1 Introduction

The laser cladding (LC) technology is an advanced processing and manufacturing technology developed in 1990s. By melting the substrate surface with the moving laser beam, and supplying powder (pre-alloying powder, mixed powder of metal and ceramic, etc.) or wire simultaneously, clad layer can be formed [1, 2]. Currently, the technology is mainly applied to surface modification of materials and remanufacturing of damaged parts and wins rapid development [3, 4].

According to the relative position between powder feeding nozzle and laser beam, one-step LC can be classified into lateral and coaxial powder-feeding. The former [5] refers to powder injection mode with certain angle relationship between axes of powder flux and the laser beam (Fig. 1), which is still widely applied in industrial production and experiment of LC process [6], such as large area cladding by a rectangular laser beam [7], inclined/vertical cladding [8] for turbine blade, cylinder body, sleeve, mold side wall, and other situations where physical interference with coaxial nozzle exits. Theoretical study for lateral powder feeding is helpful to guide the parts repair and surface modification.

The macroscopic morphology of cladding layer, such as its geometric dimensions and surface roughness, is the consequence of mutual coupling between several physical phenomena (laser beam, powder flux, molten pool) and comprehensive influences among multiple process parameters (laser power, scanning speed, powder flow rate, etc.) [9–11]. For example, collapse of the cladded wall and a wider molten pool would be caused by the gradual heat accumulation from continuous input of constant laser energy [12]. As changed energy and powder feed rate per unit length induced by accelerate/decelerate of the CNC machine or robotic arm, variation of clad height and width may appear at the beginning/end cladding or corners where speed direction turns in the complex scanning trajectories [13]. So LC process stability is hard to be guaranteed but required, and above process parameters should be adjusted in real time with the variation of process condition. The control of clad geometry is critical to the LC commercial application, especially for repair of blades with irregular surface shape. To meet this requirement, several researchers constructed closed loop control systems by using cameras or sensors [14–16]. So far in theoretical research, a great number of mathematical models have been summarized into three categories systematically [17]. The influence of process parameters on macroscopic morphology is commonly revealed by less analytical solution [18] or more numerical simulation [19–21], while there is contradiction between simplicity and accuracy for these models involved, which are difficult to be guaranteed simultaneously [22]. Moreover, statistical model by multiple regression analysis method is widely used to predict the geometry of clad layer [23–25]. But it does not help to understand the physical phenomenon involved during the process and reduce the experimental costs. In the LC production process, relatively simple mathematical model suitable for control of clad geometry is urgently needed to determine the optimal process parameters in each instant or provide an adjustment strategy reference in-house for the above closed loop control system on-process, which could make the LC industrial application easier [25].

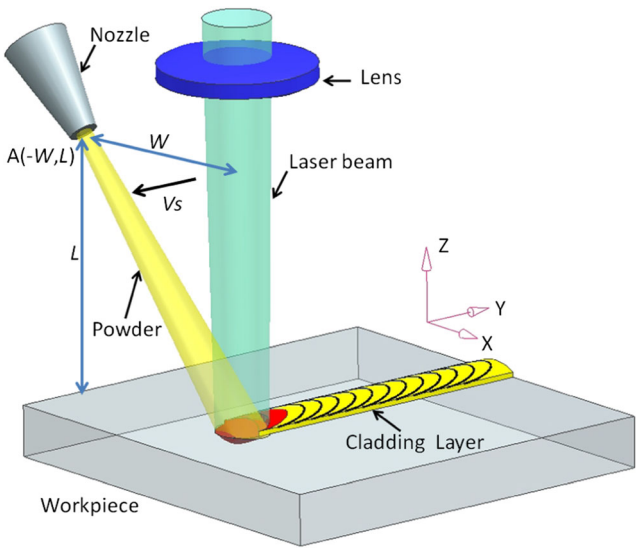

Fig. 1 Schematic of laser cladding by lateral powder-feeding

The cladding layer geometry characteristics (width, height, cross-sectional area) were governed by the distribution of powder flux, heat conduction in substrate, thermal convection inside the molten pool, and force balance on its free surface [17], including gravity, surface tension, and the impact of carrier gas. Only the cross-sectional area can be estimated under the calculation condition without energy equation involved, which is mainly determined by the amount of powder entering into the molten pool. Clad height could be obtained further as the model application in article [26]. In this paper, powder transport ratio is defined as the mass ratio of powder particles fed into the molten pool to all powders injected from the lateral powder feeding nozzle. A powder transport model for flow field with Gaussian distribution is established to derive mathematical expression of powder transport ratio and verified by experimental value of cross-sectional area indirectly and powder capturing efficiency directly. It is noteworthy that similar physical concept such as powder catchment efficiency [27], powder efficiency coefficient [28], and fraction of the powder (λ) [29] is set to approximations in the reported literature or experience. So the model in this article may also

help to improve accuracy of other related theoretical research mentioned above.

2 The model

As shown in Fig. 1, laser beam and powder stream move simultaneously, with relative velocity V_S to substrate in negative direction of y-axis. The powder nozzle is located in the position of point A ($-W$, L). With a certain initial velocity, powder particles do oblique projectile motion under gravity. The molten pool is formed on substrate by energy of laser beam, which is "obscured" by powder stream previously. Clad layer is formed by powder particles falling into the pool, which are melted by laser irradiation and heat transfer from substrate. Some other particles are lost after colliding with solid-state substrate.

Divergent powder particles from lateral nozzle are generally considered to be cylinder or Gaussian concentration distribution [30], which should be modeled separately as the real flux in experimental process has not been determined. The former has been established in article [31]. The Gaussian powder flow field, namely that, within the cross section of flow field which direction is perpendicular to the velocity of central particles, its concentration shows a normal distribution. The probability density distribution function is related to the mathematical expected value μ and standard deviation σ of Gaussian function. In this article, corresponding powder transport model is established and the expression of its powder transport ratio is derived.

For the convenience of model establishment, same assumptions with article [31] are made as follows:

(1) Projected area of powder steam on substrate surface is larger than area of the molten pool.
(2) The initial velocity of powder particles from nozzle is in the same speed but different direction. Central particles fall to the center of the moving laser spot exactly.
(3) The effect of airflow on powder particles is neglected.

2.1 Concentration of Gaussian powder flow field

In the Gaussian powder flow field (Fig. 2), powder particles from nozzle move with constant acceleration, along the parabolic trajectory under gravity and finally fall on the surface of substrate. The direction of their initial velocity V_{P0} to horizon ranges from $\theta-\varphi$ to $\theta+\varphi$. So the component initial velocity in vertical (or horizontal) direction for all powder particles varies from $V_{P0}\cdot\sin(\theta-\varphi)$ [or $V_{P0}\cdot\cos(\theta-\varphi)$] to $V_{P0}\cdot\sin(\theta+\varphi)$ [or $V_{P0}\cdot\cos(\theta+\varphi)$]. Then, these powers move with constant acceleration (/velocity) in vertical (/horizontal) direction. Within an arbitrary cross

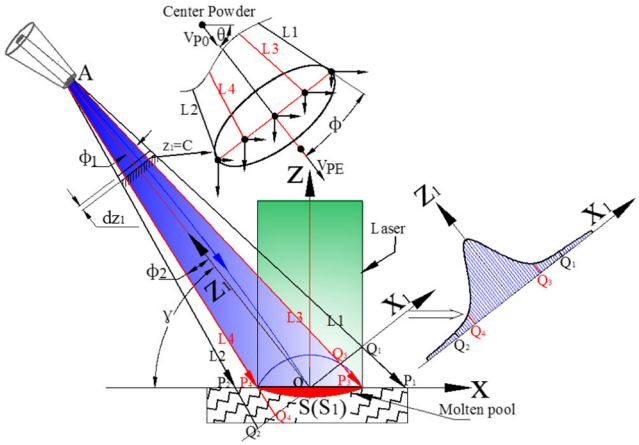

Fig. 2 Section diagram for Gaussian powder flow field

section, paralleling to the x_1-axis, the velocity field of powder particles is regularly distributed on both sides of central particles. Parabolic trajectory for particles can be simplified as a straight line trajectory. Take central particles as targets described in this model, and their instantaneous velocity at any location ($z_1 = C$) of trajectory in z_1 direction is regarded as average velocity of entire particles, which are stored in the cross section located at position C.

By law of mass conservation, mass of powder particles stored in flux space of dz_1 length in z_1 direction is given by

$$m(z_1) = V_m \cdot \frac{dz_1}{V_{\mathrm{PE}}} \tag{1}$$

Mass distribution of powder particles per unit length of stream in z_1 direction is

$$C_G(z_1) = \frac{m(z_1)}{dz_1} = \frac{V_m}{V_{\mathrm{PE}}} \tag{2}$$

Within any cross section of Gaussian flow field, paralleling to x_1-axis, powder particles are normally distributed (Fig. 2). Consequently, mass distribution of powder stream, that is, concentration in the S_1 coordinate can be

$$\begin{aligned} C_G(x_1, z_1) &= C_G(z_1)\cdot f_G(x_1;\mu,\sigma) \\ &= \frac{V_m}{\sqrt{V_{P0}^2 + 2g(L_{AO}-z_1)\sin\gamma}} \cdot \frac{1}{\sigma\sqrt{2\pi}} \exp\left[-\frac{(x_1-\mu)^2}{2\sigma^2}\right] \end{aligned} \tag{3}$$

where the expression of V_{PE} can be confirmed by Eq. (16) in article [31].

2.2 Calculation of powder transport ratio

Intersection of powder flow field boundary $L(i)$ and x_1-axis (Fig. 2) is set as $Q(i)$. m_3 and m_4 are defined as mass of powder

particles stored on Q_3Q_4 and Q_1Q_2 segments, respectively. Particles with mass of m_3 would fall into the molten pool as mass of m_4 transported from nozzle totally. Then, the solution of powder transport ratio for Gaussian distribution can be transformed into calculation for the ratio of m_3 to m_4 in steady-state powder flow field.

As the same initial condition of powder feeding (relative position and inclination angle of the powder nozzle, initial velocity of powders), cylindrical [31] and Gaussian powder flow field should have the same geometric boundary conditions. The difference between them is only particles concentration distribution within any cross section of powder flux perpendicular to the velocity direction of central particles. Therefore, boundary conditions of this model can be substituted by corresponding formula in article [31]. Some other boundary conditions are solved as follows,

For RtΔAOQ_3 and RtΔAOQ_4,

$$x_1(Q_3) = L_{AO}\cdot tg\varphi_1 \tag{4}$$

$$x_1(Q_4) = -L_{AO}\cdot tg\varphi_2 \tag{5}$$

where expressions of L_{AO}, φ_1, and φ_2 have been derived by Eqs. (10, 11, 13) in article [31]. Then,

$$x_1(Q_3) = \frac{L\cdot D}{W\cdot D + 2\left(L^2+W^2\right)}\sqrt{L^2+W^2} \tag{6}$$

$$x_1(Q_4) = \frac{L\cdot D}{W\cdot D - 2\left(L^2+W^2\right)}\sqrt{L^2+W^2} \tag{7}$$

In addition, by geometry relations of powder flow field boundary

$$x_1(Q_1) = L_{AO}\cdot tg\varphi + D_{jet}/2 = \sqrt{L^2+W^2}\cdot tg\varphi + D_{jet}/2 \tag{8}$$

$$x_1(Q_2) = -L_{AO}\cdot tg\varphi - D_{jet}/2 = -\sqrt{L^2+W^2}\cdot tg\varphi - D_{jet}/2 \tag{9}$$

In Gaussian powder flow field (Fig. 2), particles obey normal distribution, that is $X\sim N(\mu,\sigma^2)$. According to the symmetry of powder flow field,

$$\mu = 0 \tag{10}$$

Also, based on the 3σ principle of normal distribution function, about 99.730020% of the area locates within the range of three standard deviations on both sides of the mathematical expectation,

$$3\sigma = |x_1(Q_1) - x_1(Q_2)|/2 \tag{11}$$

where $x_1(Q_1)$ and $x_1(Q_2)$ can be confirmed by Eqs. (8 and 9), then,

$$\sigma = \frac{1}{3}tg\varphi\sqrt{L^2+W^2} + D_{jet}/6 \tag{12}$$

Finally, related parameters are substituted by Eqs. (3, 6–9), analytical solution of powder transport ratio with Gaussian distribution can be given as follows

$$m_3 = C\cdot L_{Q_3Q_4} = \int_{x_1(Q_4)}^{x_1(Q_3)} C_G(x_1,z_1)\cdot dx_1\Big|_{Z_1=0} \tag{13}$$

$$m_4 = C\cdot L_{Q_1Q_2} = \int_{x_1(Q_2)}^{x_1(Q_1)} C_G(x_1,z_1)\cdot dx_1\Big|_{Z_1=0} \tag{14}$$

$$\xi_{PT}^G = \frac{m_3}{m_4}\times 100\% \tag{15}$$

3 Calculation of the cross-sectional area for clad layer

An important application of powder flow study is to control or predict morphology of the cladding layer. If only mass of powder is considered, under the condition of sufficient laser energy, all particles falling into the molten pool would form the clad layer. Cross-sectional area (S) could be estimated by the model above. The relationship between ξ and S, formed by particles falling into the molten pool, has been derived in article [31] as follows,

$$S_{PT}^G = \frac{M_{PT}}{\rho\cdot 1} = \frac{V_m\cdot\xi_{PT}^G}{V_S\cdot\rho} \tag{16}$$

where $\xi^G{}_{PT}$ could be confirmed by Eq. (15), and $S^G{}_{PT}$ characterized the theoretical value of the cross-sectional area from the perspective of powder mass transported.

In addition, as all powders from nozzle are transported into the molten pool, that is, $\xi^G{}_{PT}$ is 100%, maximum of cross-sectional area S_{P0} is given by

$$S_{P0} = \frac{V_m}{V_S\cdot\rho} = \frac{S_{PT}^G}{\xi_{PT}^G} \tag{17}$$

For the single track cladding process of TC11 titanium alloy powder, $S^G{}_{PT}$ corresponding to 11 set of process schemes could be calculated and is listed in Table 1. As the treatment method for initial conditions in article [31], width of the molten pool corresponding to each parameter is wholly set as diameter (D) of the laser beam. Other input variables in this model are determined by experimental conditions, and substitution values are shown as follows:

$$D = 0.3\ \text{cm}; D_{jet} = 0.15\ \text{cm}; g = 9.8\ \text{m/s}^2; L = 8.9\ \text{mm}; V_{P0} = 26.76\ \text{cm/s}; W = 5.2\ \text{mm}; \varphi = 15.8^\circ; \theta = 45.8^\circ; \rho = 4.48\ \text{g}\cdot\text{cm}^{-3}.$$

Table 1 Theoretical results for Gaussian powder flow field and experimental value

Test no.	V_m (g/min)	P (W)	V_S (mm/s)	D (mm)	ξ_L (%)	ξ_φ (%)	ξ^G_{PT} (%)	S^G_{PT} (mm^2)	S_{P0} (mm^2)	S (mm^2)
1#	3.233	1000	3.5	3	54.15	45.56	71.4	2.453	3.436	0.249
2#		1200								0.537
3#		1500								1.278
4#		1200	3					2.862	4.009	0.918
5#	4.07	1200	3					3.604	5.047	1.104
6#			3.5					3.089	4.326	0.894
7#			4					2.703	3.785	0.701
8#		1500	3.5					3.089	4.326	1.528
9#	4.89	1500	3.5					3.711	5.198	1.953
10#		1200								1.218
11#			3					4.33	6.064	1.519

As ξ^G_{PT} is obtained by Eq. (15), process parameters (Table 1) for V_S and V_m are brought into Eq. (16) to solve the theoretical value S^G_{PT}. After verified by experiment, theoretical results would be modified by the true width (D_1) of the molten pool.

4 Experimental procedure

The purpose of experiments is to verify the correctness of the theoretical model in this paper, which is carried out from aspects of qualitative and quantitative research. For the laser cladding of lateral powder feeding, experimental procedure is listed as follows.

(1) A high-speed COMS camera (2100 megapixels) is used to capture the macroscopic distribution characteristics of the powder flux emitted from the nozzle under the condition of 3.23 g/min, 4.07 g/min, and 4.89 g/min powder feed rate in Table 1. The result is shown in Fig. 6a–c.

(2) The 1-mm-thick transparent PVC plastic plate was placed on a horizontal plane 125 mm away from the vertical powder feeding nozzle to collect the powder. Particle distribution of the powder flux in the XOY plane could be observed directly. To minimize the interference of particle displacement induced by rigid collision with the PVC plate, the double-sided adhesive is pre-applied to the latter surface, which could adhere more particles in the feeding process. The powder feeding time was unified to 5 s, and this experiment was carried out also using the above three powder feeding rates in Table 1. Then, the two-dimensional slice of the powder flow in the horizontal direction is lined on the yellow bottom, displayed in Fig. 6d–f.

(3) Corresponding to theoretical calculation of cross-sectional area in Sect. 3, this experimental verification program is just the same as article [31]. Experiment of laser cladding by lateral powder feeding is conducted in a single track, by using laser power P, scanning speed V_S, and powder feed rate V_m as variables (Table 1). Other process and condition parameters are set as constants. TC11 titanium alloy powders are deposited by CO_2 laser on TC4 substrate with argon protective atmosphere. After the experiment, mean values of cross-sectional area are measured and calculated by the MIAPS-M image analysis software. Macroscopic morphology of clad layer for 2# and 8# is present in Fig. 3 and compared with 1# and 6# [31]. The difference of each group experimental results is mainly reflected in height, width and cross sectional area S of the clad layer. Consequently, experimental measurement result S is taken as a comparison item and listed in Table 1 as the energy equation is not involved in this theoretical model.

(4) As the theoretical results ξ^G_{PT} and S^G_{PT} would be modified by the actual boundary condition of molten pool width (D_1), the model also need to be verified for the prediction of ξ^G_{PT} as a function of pool width variation, so the powder efficiency is measured by weighting method directly in this experiment. In Fig. 4, a powder collection device was equipped by two steel sheets (100 mm × 10 mm × 0.3 mm), springs and hexagon socket bolts. Distance of the two sheets can be adjusted by bolts which simulating different width of the molten pool. Thus, powder particles trapped in this device could be seen as cladding layer and weighted to calculate powder efficiency further. The experimental test consist of a series of TC11 titanium alloy powder injections with 4.07 g/min powder feed rate during 10 s, over different widths of the particle trap which is set as ten groups in this work and range from 1.5 to 6 mm, 0.5 mm increased. All tests were programmed with the same powder injection parameters as data listed in Sect. 3. Before this test,

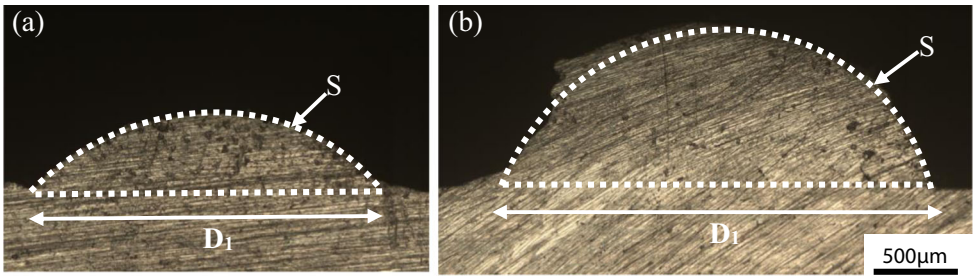

Fig. 3 Morphology photos of laser cladding layer. **a** 2#. **b** 8#

center point of the powder flux should be determined, according which the collecting device is placed symmetrically and marked as a fixed position. Then, nozzle outlet is raised by 10 mm so that above center point falls on the upper surface of the device, considered as a working plane. The mass ratio of the collected powder to the total powder from nozzle is the capturing efficiency, which is distributed in Fig. 7. In addition, weight difference between two consecutive measurements is the weight of powder stored in the corresponding space difference. Powder flux distribution on this working plane determined by injection parameters mentioned could also be obtained and is illustrated in Fig. 8. Approximately, the powder particles are evenly distributed on the left and right sides in each space difference, so the graphic is symmetrical.

5 Results and discussion

5.1 Experimental verification and modification for the model

The judgment process of model authenticity is mainly based on numerical comparison from experiment (3) and (4), supplemented by photo observation from experiment (1) and (2). From the perspective of powder mass transported, cross-sectional area S^{G}_{PT} of clad layer formed by powders falling into the molten pool could be estimated by this model. By comparing with experimental value S, the model with Gaussian distribution is verified indirectly. In addition, powder transport ratio ξ^{G}_{PT1} modified by previous step can also be confirmed directly by powder efficiency measured in experiment.

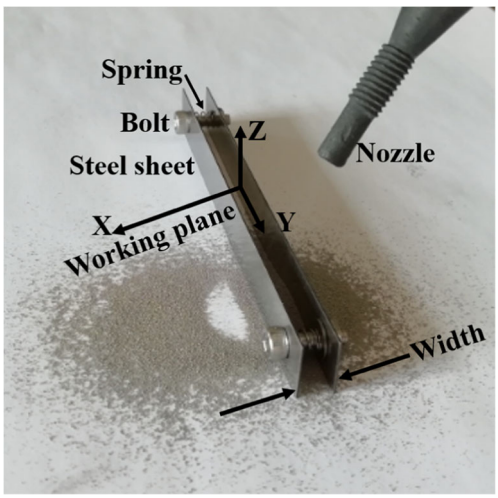

Fig. 4 Powder collection device

Theoretical and experimental results are listed in Table 1. Since the width of molten pool is set to 3 mm uniformly, same geometric boundary conditions are substituted during each calculation for different parameters, and ξ^{G}_{PT} keeps a constant. Error is occurred by the approximate treatment. Thus, S^{G}_{PT} deviates from S. In order to modify theoretical calculations, actual width of the molten pool D_1 is measured in Fig. 3 through standard metallographic method, then brought into the model to calculate modification values of ξ^{G}_{PT1} and S^{G}_{PT1}, which are listed in Table 2.

For easy comparison of above data, experimental values S are sequenced in ascending order and distributed evenly in the horizontal axis (Fig. 5). Then, theoretical values such as S_{P0}, S^{G}_{PT}, S^{G}_{PT1}, and S^{C}_{PT1} (calculated in article [31]) are distributed as the same order. Five regression lines are drawn by simple liner fitting on each group of scatter plot in Fig. 5.

By comparing of S, S^{G}_{PT}, and S^{G}_{PT1}, the powder transport model with Gaussian distribution is in satisfactory agreement with actual experiment. With the change of process parameters, variation of the cross-sectional area (S^{G}_{PT}, S^{G}_{PT1}) calculated by this model is in accordance with the trend of experimental data (S). And theoretical modification value S^{G}_{PT1} is closer than S^{G}_{PT} to the experimental value S.

The maximum S_{P0} is also calculated by Eq. (17) and distributed in Fig. 5, which characterizes the size of cross-sectional area formed by all particles transported from nozzle, and shows a positive correlation with S^{G}_{PT} and S^{G}_{PT1}. Proportional relationship of S^{G}_{PT1} to S_{P0} represents ξ^{G}_{PT1}. Furthermore, powder efficiency is the mass ratio of cladding layer (S) to the total powders (S_{P0}). So it is all reasonable for the model verification by comparing of powder efficiency directly or cross sectional area indirectly. And the relative value R of powder efficiency to ξ^{G}_{PT1} can be revealed by S to S^{G}_{PT1}.

Table 2 Theoretical modified results for Gaussian powder flow field

Test no.	V_m (g/min)	P (W)	V_s (mm/s)	D_1 (mm)	ξ_{L1} (%)	ξ^G_{PT1} (%)	S^G_{PT1} (mm2)	S (mm2)
1#	3.233	1000	3.5	1.673	30.2	44.71	1.536	0.249
2#		1200		2.048	36.97	53.27	1.831	0.537
3#		1500		2.587	46.7	64.17	2.205	1.278
4#		1200	3	2.272	41.01	58.02	2.326	0.918
5#	4.07	1200	3	2.208	39.86	56.68	2.861	1.104
6#			3.5	2.003	36.15	52.28	2.262	0.894
7#			4	1.872	33.79	49.34	1.867	0.701
8#		1500	3.5	2.546	45.96	63.42	2.744	1.528
9#	4.89	1500	3.5	2.433	43.92	61.24	3.183	1.953
10#		1200		1.928	35	50.61	2.631	1.218
11#			3	2.127	38.39	54.97	3.333	1.519

The energy equations are not involved in the calculation of S^G_{PT1}, formed by particles falling into the molten pool. Whether these particles are fully melted by laser have not been taken into consideration. Actually, as insufficient energy in local area of the molten pool, part of particles would be lost after colliding with others. By its definition, ξ^G_{PT1} is inevitability larger than the actual powder efficiency, resulting in a higher value of S^G_{PT1} than experimental results S. Especially as the laser liner energy (P/V_s) is smaller, such deviation degree is greater. As the similar variation of theoretical and experimental values, the significance of this powder transported model lies in predicting trends with process parameters quantitatively and estimating approximation for the actual cross-sectional area and powder efficiency. More accurate solution of S would be obtained by the product of an empirical coefficient R mentioned above and the theoretical result S^G_{PT1}.

By comparing data distribution of S^G_{PT1}, S^C_{PT1}, S, and their regression lines, although S^C_{PT1} is closer to S than S^G_{PT1}, the trend of S^G_{PT1} affected by process parameters is still more realistic as similar slope of regression line between S^G_{PT1} and S. So, it can be regarded that concentration distribution of powder flux in actual trends to be Gaussian type rather than uniformity, which could be proved qualitatively by photographs in Fig. 6 whether for vertical camera shooting or two-dimensional horizontal slice. The reason for relatively small error induced by S^C_{PT1} may be associated with the restriction of energy factor on the mass or cross-sectional area of clad layer. In addition, with the increase of powder feed rate V_m, the divergence angle of powder flux remains unchanged almost in Fig. 6. It is reasonable to neglect the influence of V_m on the boundary conditions in the theoretical calculation.

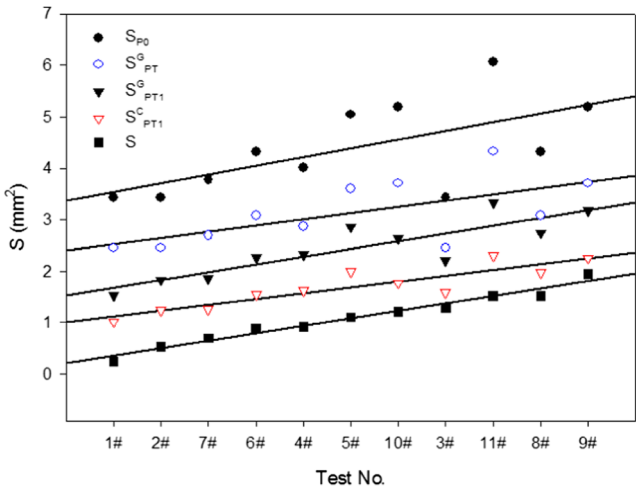

Fig. 5 Data distribution of theoretical and experimental results for cross-sectional area

Quantitative verification for powder transport ratio ξ^G_{PT1} is carried out by comparing with powder efficiency (S/S_{P0}) by experiment (3) and capturing efficiency by experiment (4). Widths of the molten pool from 0 to 7 mm, increased by 0.2 mm, are substituted into the model, and variation curve of ξ^G_{PT1} is drawn in Fig. 7. Experimental data is also distributed with the width. As mentioned before, a certain degree of deviation exists between power efficiency and ξ^G_{PT1} due to loss of particle collision in the local area of insufficient energy. With the increase of laser liner energy or molten pool width, powder efficiency approximates ξ^G_{PT1} gradually. The capturing efficiency value is the experimental results corresponding to the theoretical ξ^G_{PT1}, both of which have the similar trend with width. It seems that more particles are captured than theoretical prediction in the narrow range of molten pool, while less in the wider range. In addition, the capturing efficiency should be consistently greater than the powder efficiency as the energy factor.

The above difference can be more intuitively reflected from mass distribution of powder flux. According to the curve in Fig. 7, mass of powder stored in each symmetrical width range of 0.2 mm can be calculated, and then divided equally into the left and right intervals as the approximation method in experiment (4). Under the condition of 4.07 g/min powder feed rate during 10 s, particle mass distribution on working plane, determined by experimental

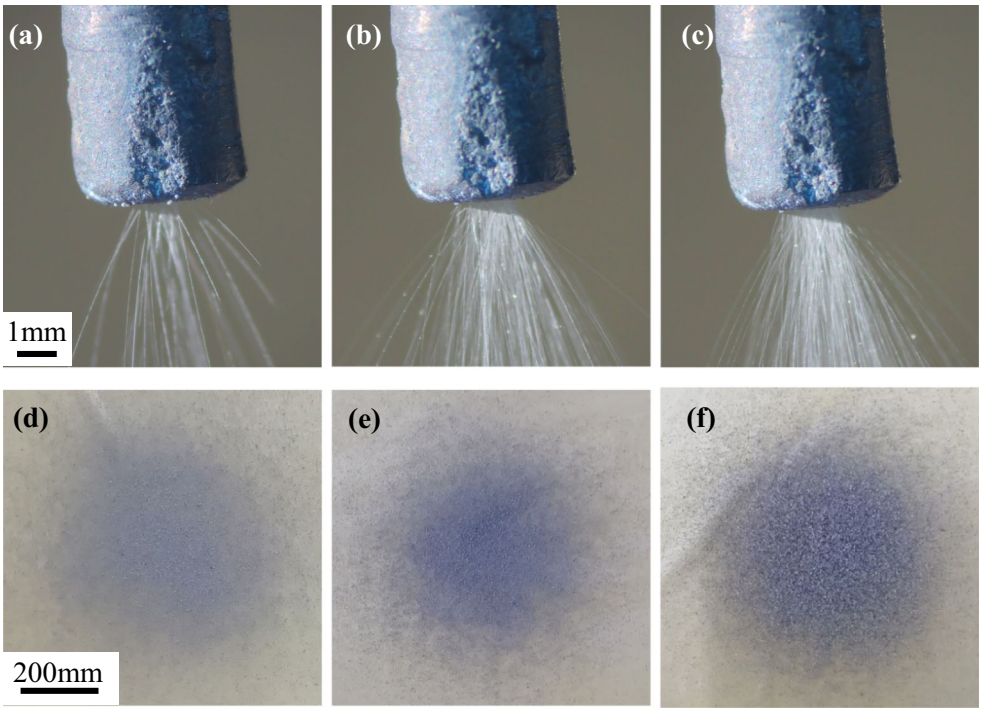

Fig. 6 Photographs of powder flux. **a** 3.23 g/min, vertical shooting. **b** 4.07 g/min, vertical shooting. **c** 4.89 g/min, vertical shooting. **d** 3.23 g/min, horizontal slice distanced 125 mm from nozzle, 5 s powder injection. **e** 4.07 g/min, horizontal slice distanced 125 mm from nozzle, 5 s powder injection. **f** 4.89 g/min, horizontal slice distanced 125 mm from nozzle, 5 s powder injection

injection parameters, is illustrated in Fig. 8. As its symmetry, this is equivalent to the concentration distribution in the S_1 coordinate of Fig. 2 and photographed in Fig. 6d–f. The fundamental reason for deviation between the model and experiment lies in the inconsistency of their descriptions on powder flux characteristics. The actual powder flux is more concentrated in the central area and dispersed at the edge. Nevertheless, variation of ξ^{G}_{PT1} with molten pool width calculated by this Gaussian model is more accurate than the cylindrical type [31].

5.2 Influence of parameters on powder transport ratio

Cross-sectional area S^{G}_{PT1} (↗) is determined by powder feed rate V_m (↗), powder transport ratio ξ^{G}_{PT1} (↗), and laser scanning speed V_S (↘) in Eq. (16). By the above analysis, ξ^{G}_{PT1} depends on the molten pool width D_1 directly and shows a positive correlation, which would be affected further by V_m, V_S, and laser power P [25]. The mechanism of above process parameters on morphology of the cladding layer is complicated, so the influence on ξ^{G}_{PT1} deserves to be discussed firstly. According V_m, ξ^{G}_{PT1} values in Table 2 are distributed, and groups with same P and V_S are curved in Fig. 9. From these

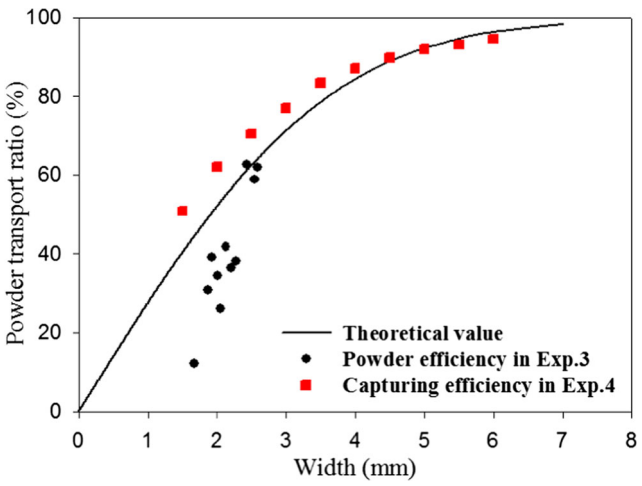

Fig. 7 Curve of powder transport ratio with molten pool width

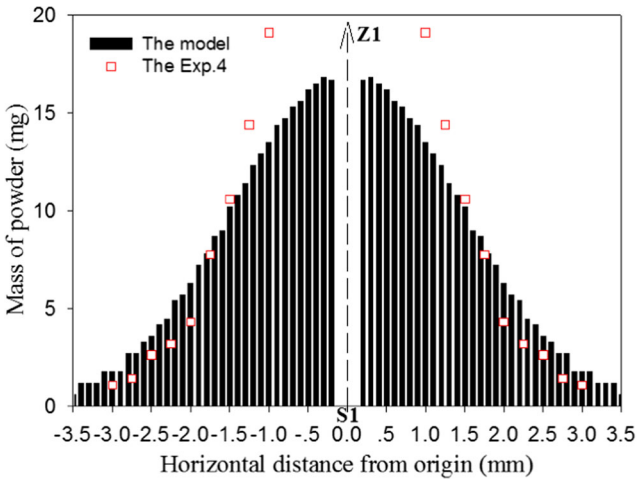

Fig. 8 Powder flux distribution with 4.07 g/min powder feed rate during 10 s

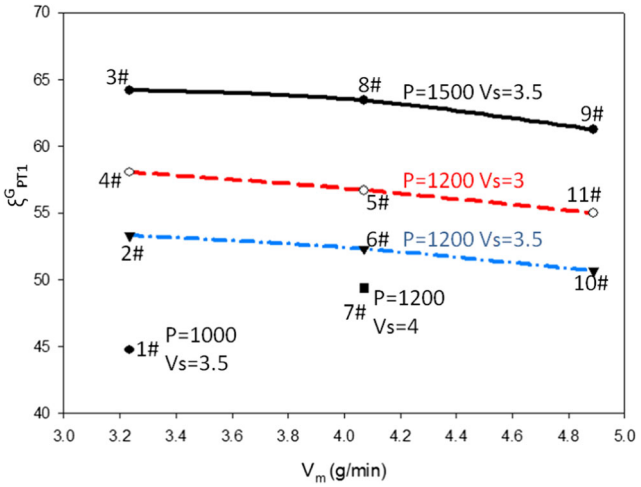

Fig. 9 Curve of the powder transport ratio with powder feed rate

three curves, ξ^G_{PT1} is decreased slowly with V_m. Part of laser energy is absorbed or scattered by the flying particle. D_1 would be decreased with the increased powder concentration as the remaining energy passing through the particle cloud is attenuated [24]. Moreover, ξ^G_{PT1} increases with laser power (1#, 2#, 3#) and decreases with scanning speed (5#, 6#, 7#). By comparing ξ^G_{PT1} (Fig. 9) and ξ^C_{PT1} (Fig. 5 from article [31]), curve variation have the similar trends with V_m (or D_1) but different degrees as concentration distribution difference between Gaussian and cylindrical powder flux.

5.3 Comparison with the geometric model

Powder efficiency [30] is estimated by geometric relationship of powder flow field boundaries, in which particle concentration distribution is not involved. A comparison between such geometric model and the Gaussian model is present. In the same space of powder flux, ξ_L and ξ_φ are defined as powder efficiency for length and angle, respectively. Analytical solutions can be confirmed by Eqs. (18 and 19) and are listed in Table 1. Modified powder efficiency for length ξ_{L1} are calculated in Table 2 as the actual molten pool width are brought into Eq. (18)

$$\xi_L = \frac{D}{|P_1P_2|} \tag{18}$$

$$\xi_\varphi = \frac{\varphi_1 + \varphi_2}{2\varphi} \tag{19}$$

where mathematical expressions of $|P_1P_2|$, φ_1, and φ_2 are given by Eqs. (4, 5, 10, 11) in article [31].

By comparing ξ^G_{PT}, ξ_L, and ξ_φ in Table 1 and ξ^G_{PT1} and ξ_{L1} in Table 2, powder transport ratio is higher than powder efficiency for length and angle, which is different from cylindrical powder flow field. Under the experimental condition, in which powder flux is trend to be Gaussian distributed, large error for powder efficiency calculated by the above geometric model is caused inevitably.

6 Conclusion

(1) On the basis of some physical assumptions, according to the law of mass conservation and motion equation in physics, a powder transport model for flow field with Gaussian distribution and a mathematical expression of powder transport ratio are proposed.
(2) Cross-sectional area of clad layer is calculated to verify the model indirectly. As the energy factor is not involved, theoretical and its modified values are higher than experiment result which is closer to the latter, but all of them have similar variation trend with process parameters. The model with Gaussian distribution can be used for fundamental research of actual powder flow field.
(3) Powder transport ratio is confirmed directly by experiments. Deviation exists between powder transport ratio and powder efficiency, which is reduced with increased width of molten pool. Moreover, variation of powder transport ratio and capturing efficiency with molten pool width are similar but different as their slightly inconsistent description on the powder flux distribution. Compared with theoretical model, the actual powder flux is more concentrated in the central area and dispersed at the edge.
(4) Powder transport ratio decreases with powder feed rate or laser scanning speed and increases with laser power.
(5) Powder transport ratio for flow field with Gaussian distribution is larger than powder efficiency for length and angle.
(6) Actual powder flow field in this article trends to be distributed as Gaussian function.

Acknowledgements Technical advices from Yongzhong Zhang, Yantao Liu, and Mingkun Liu in GRINM are greatly appreciated.

Funding information This work is financially supported by Basic Scientific Research Service Fee of Central University (No. 3142015012) and Langfang Science and Technology Research Development Program (No. 2017011035).

References

1. Tian XY, Sun B, Heinrich JG, Li DC (2012) Scan pattern, stress and mechanical strength of laser directly sintered ceramics. Int J Adv Manuf Technol 64(1–4):239–246. https://doi.org/10.1007/s00170-012-3994-6
2. Chivel YA (2018) A new method of selective laser cladding. Tech Phys Lett 44(11):1045–1048. https://doi.org/10.1134/S1063785018110196

3. Zhu GX, Shi SH, Fu GY, Shi JJ, Yang S, Meng WD, Jiang FB (2017) The influence of the substrate-inclined angle on the section size of laser cladding layers based on robot with the inside-beam powder feeding. Int J Adv Manuf Technol 88(5–8):2163–2168. https://doi.org/10.1007/s00170-016-8950-4
4. Plooy RD, Akinlabi ET (2018) Analysis of laser cladding of titanium alloy. Mater Today: Proceed 5(9):19594–19603. https://doi.org/10.1016/j.matpr.2018.06.322
5. Wirth F, Wegener K (2018) Simulation of the multi-component process gas flow for the explanation of oxidation during laser cladding. Addit Manuf 24:249–256. https://doi.org/10.1016/j.addma.2018.10.010
6. Nagulin KY, Iskhakov FR, Shpilev AI, Gilmutdinov AK (2018) Optical diagnostics and optimization of the gas-powder flow in the nozzles for laser cladding. Opt Laser Technol 108:310–320. https://doi.org/10.1016/j.optlastec.2018.07.001
7. Liu S, Zhang Y, Kovacevic R (2015) Numerical simulation and experimental study of powder flow distribution in high power direct diode laser cladding process. Lasers Manuf Mater Process 2(4):199–218. https://doi.org/10.1007/s40516-015-0015-2
8. Paul CP, Mishra SK, Kumar A, Kukreja LM (2013) Laser rapid manufacturing on vertical surfaces: analytical and experimental studies. Surf Coat Technol 224(15):18–28. https://doi.org/10.1016/j.surfcoat.2013.02.044
9. Goodarzi DM, Pekkarinen J, Salminen A (2017) Analysis of laser cladding process parameter influence on the clad bead geometry. Weld World 61(5):883–891. https://doi.org/10.1007/s40194-017-0495-0
10. Khamidullin BA, Tsivilskiy IV, Gorunov AI, Gilmutdinov AK (2019) Modeling of the effect of powder parameters on laser cladding using coaxial nozzle. Surf Coat Technol 5(9):19594–19603. https://doi.org/10.1016/j.surfcoat.2018.12.002
11. Liu HM, Li MB, Qin XP, Huang S, Hong F (2019) Numerical simulation and experimental analysis of wide-beam laser cladding. Int J Adv Manuf Technol 100(1–4):237–249. https://doi.org/10.1007/s00170-018-2740-0
12. Moralejo S, Penaranda X, Nieto S, Barrios A, Arrizubieta I, Tabernero I, Figueras J (2017) A feedforward controller for tuning laser cladding melt pool geometry in real time. Int J Adv Manuf Technol 89(1–4):821–831. https://doi.org/10.1007/s00170-016-9138-7
13. Arrizubieta JI, Martinez S, Lamikiz A, Ukar E, Arntz K, Klocke F (2017) Instantaneous powder flux regulation system for laser metal deposition. J Manuf Process 29:242–251. https://doi.org/10.1016/j.jmapro.2017.07.018
14. Montero J, Rodríguez A, Amado JM, Yanez AJ (2016) Inspection of powder flow during LMD deposition by high speed imaging. Phys Procedia 83:1319–1328. https://doi.org/10.1016/j.phpro.2016.08.139
15. Ding YY, Warton J, Kovacevic R (2016) Development of sensing and control system for robotized laser-based direct metal addition system. Addit Manuf 10:24–35. https://doi.org/10.1016/j.addma.2016.01.002
16. Smurov I, Doubenskaia M, Grigoriev S, Nazarov A (2012) Optical monitoring in laser cladding of Ti6Al4V. J Therm Spray Technol 21(6):1357–1362. https://doi.org/10.1007/s11666-012-9808-4
17. Kovalev OB, Bedenko DV, Zaitsev AV (2018) Development and application of laser cladding modeling technique: from coaxial powder feeding up to the surface deposition and bead formation. Appl Math Model 57:339–359. https://doi.org/10.1016/j.apm.2017.09.043
18. Cheikh HE, Courant B, Branchu S, Hascoët JY, Guillén R (2012) Analysis and prediction of single laser tracks geometrical characteristics in coaxial laser cladding process. Opt Lasers Eng 50(3):413–422. https://doi.org/10.1016/j.optlaseng.2011.10.014
19. Liu H, Hao JB, Yu G, Yang HF, Wang LW, Han ZT (2016) A numerical study on metallic powder flow in coaxial laser cladding. J Appl Fluid Mech 9(5):2247–2256. https://doi.org/10.18869/acadpub.jafm.68.236.25632
20. Parekh R, Buddu RK, Patel RI (2016) Multiphysics simulation of laser cladding process to study the effect of process parameters on clad geometry. Proced Technol 23:529–536. https://doi.org/10.1016/j.protcy.2016.03.059
21. Koruba P, Wall K, Reiner J (2018) Influence of processing gases in laser cladding based on simulation analysis and experimental tests. Abbreviation 74:719–723. https://doi.org/10.1016/j.procir.2018.08.025
22. Tabernero I, Lamikiz A, Martínez S, Ukar E, Lacalle L (2012) Geometric modelling of added layers by coaxial laser cladding. Phys Procedia 39:913–920. https://doi.org/10.1016/j.phpro.2012.10.116
23. Farahmand P, Kovacevic R (2014) Parametric study and multicriteria optimization in laser cladding by a high power direct diode laser. Lasers Manuf Mater Process 1(1–4):1–20. https://doi.org/10.1007/s40516-014-0001-0
24. Bourahima F, Helbert AL, Rege M, Ji V, Solas D, Baudin T (2019) Laser cladding of Ni based powder on a Cu-Ni-Al glassmold: influence of the process parameters on bonding quality and coating geometry. J Alloys Compd 771(15):1018–1028. https://doi.org/10.1016/j.jallcom.2018.09.004
25. Lei K, Qin X, Liu H, Mao N (2018) Analysis and modeling of melt pool morphology for high power diode laser cladding with a rectangle beam spot. Opt Lasers Eng 110:89–99. https://doi.org/10.1016/j.optlaseng.2018.05.022
26. Tabernero I, Lamikiz A, Ukar E, Lacalle L, Angulo C, Urbikain G (2010) Numerical simulation and experimental validation of powder flux distribution in coaxial laser cladding. J Mater Process Technol 210(15):2125–2134. https://doi.org/10.1016/j.jmatprotec.2010.07.036
27. Kumar A, Paul CP, Pathak AK, Bhargava P, Kukreja LM (2012) A finer modeling approach for numerically predicting single track geometry in two dimensions during laser rapid manufacturing. Opt Laser Technol 44(3):555–565. https://doi.org/10.1016/j.optlastec.2011.08.026
28. Oliveira U, Ocelík V, De Hosson JTM (2005) Analysis of coaxial laser cladding processing conditions. Surf Coat Technol 197(2–3):127–136. https://doi.org/10.1016/j.surfcoat.2004.06.029
29. Lalas C, Tsirbas K, Salonitis K, Chryssolouris G (2007) An analytical model of the laser clad geometry. Int J Adv Manuf Technol 32(1–2):34–41. https://doi.org/10.1007/s00170-005-0318-0
30. Frenk A, Vandyoussefi M, Wagnière JD, Kurz W, Zryd A (1997) Analysis of the laser-cladding process for stellite on steel. Metall Mater Trans B 28(3):501–508. https://doi.org/10.1007/s11663-997-0117-0
31. Gong XY, Zhang YZ, Liu MK (2013) Powder transport model for laser cladding by lateral powder feeding: I. Powder flow field with cylindrical distribution. Int J Adv Manuf Technol 67(9–12):2501–2509. https://doi.org/10.1007/s00170-012-4667-1